

Tuning the BCS-BEC crossover of electron-hole pairing with pressure

Yuhao Ye¹, Jinhua Wang¹, Pan Nie¹, Huakun Zuo¹, Xiaokang Li¹, Kamran Behnia², Zengwei Zhu^{1,*}, and Benoît Fauqué³
(1) Wuhan National High Magnetic Field Center and School of Physics,
Huazhong University of Science and Technology,
Wuhan 430074, China
(2) Laboratoire de Physique et d'Etude des Matériaux (CNRS)
ESPCI Paris, PSL Research University, 75005 Paris, France
(3) JEIP, USR 3573 CNRS, Collège de France,
PSL University, 11, place Marcelin Berthelot,
75231 Paris Cedex 05, France

(Dated: April 30, 2024)

In graphite, a moderate magnetic field confines electrons and holes into their lowest Landau levels. In the extreme quantum limit, two insulating states with a dome-like field dependence of their critical temperatures are induced by the magnetic field. Here, we study the evolution of the first dome (below 60 T) under hydrostatic pressure up to 1.7 GPa. With increasing pressure, the field-temperature phase boundary shifts towards higher magnetic fields, yet the maximum critical temperature remains unchanged. According to our fermiology data, pressure amplifies the density and the effective mass of hole-like and electron-like carriers. Thanks to this information, we verify the persistent relevance of the BCS relation between the critical temperature and the density of states in the weak-coupling boundary of the dome. In contrast, the strong-coupling summit of the dome does not show any detectable change with pressure. We argue that this is because the out-of-plane BCS coherence length approaches the interplane distance that shows little change with pressure. Thus, the BCS-BEC crossover is tunable by magnetic field and pressure, but with a locked summit.

I. INTRODUCTION

In 1961, Mott made the observation that Coulomb attraction between electrons and holes of a semi-metal can form bound pairs known as excitons [1]. Knox then proposed that a sufficiently large exciton binding energy would lead to an insulating state, quite distinct from an ordinary band insulator [2]. Later, Keldysh and Kozlov [3] remarked that if the carriers are sufficiently light and not too dilute, the bosonic excitons would have a sizeable Bose-Einstein condensation (BEC) temperature. Starting from these two postulates, the early research on excitonic insulators proposed that this state of matter should be sought near a semimetal to semiconductor transition and produced a phase diagram, which we reproduce in Fig. 1a (See figure 3 in [4], figure 1 in [5] and figure 3 in [6]). In 1985, Nozières and Schmitt-Rink [7] demonstrated that the transition between the strong-coupling limit (the BEC of composite bosons, either excitons or Cooper pairs) to the weak-coupling limit (the Bardeen-Cooper-Schrieffer or BCS) is smooth. The latter corresponds to the long tail on the left hand side of the excitonic dome in Fig. 1a.

Graphite, a semimetal with an equal density of electrons and holes ($n = p \approx 3 \times 10^{18} \text{cm}^{-3}$ [8]), suffers a phase transition at high magnetic field [9], which has been under exploration during four decades [10–19]. The experimental discovery in 1981 [20] led to an immediate theoretical identification of this state [10] as a charge density wave (CDW). Indeed, confining all carriers to their lowest Landau level opens the way to a nesting instabil-

ity. This is the case of graphite in presence of a magnetic field exceeding 7.4 T [21, 22]. In 1998, Yaguchi and Singleton discovered that the field-induced state abruptly ends at 53 T [11] (see Fig. 1b). In 2013, Fauqué *et al.* found that the first dome is followed by a second dome [15] and that the *c*-axis resistance shows an activated behavior in both domes. These observations challenged the CDW scenario. In 2017, Zhu *et al.* highlighted the similarity between the experimental (Fig. 1b) phase diagram of graphite and the theoretical (Fig. 1a) phase diagram of an excitonic insulator [23]. The accumulated experimental evidence since then indicates that while the transition can be described by a BCS picture of electron-hole pairing at low field [12, 16, 19], the summit of the dome corresponds to the temperature at which the thermal wavelength and the interbosonic distance match [18], as expected for a BEC transition [24].

Besides excitons [25–31], BEC has been reported for other bosonic systems, like photons [32, 33], microcavity polaritons [34, 35], and magnons [36–38]. On the other hand, the BCS-BEC crossover [39, 40], which requires tuning either distance between the bosons or the BCS correlation length, has been mainly studied in ultracold Fermi gases, thanks to the Feshbach resonance [41–48]. The possibility of the existence of BEC-BCS crossover in superconductors has been proposed for cuprates [39], organic superconductors [49, 50], iron-based superconductors [51, 52], gate-controlled two-dimensional superconducting devices [53, 54], interfacial superconductors [55, 56], magic-angle twisted superconducting bilayer [57, 58] trilayer graphene [59, 60], and

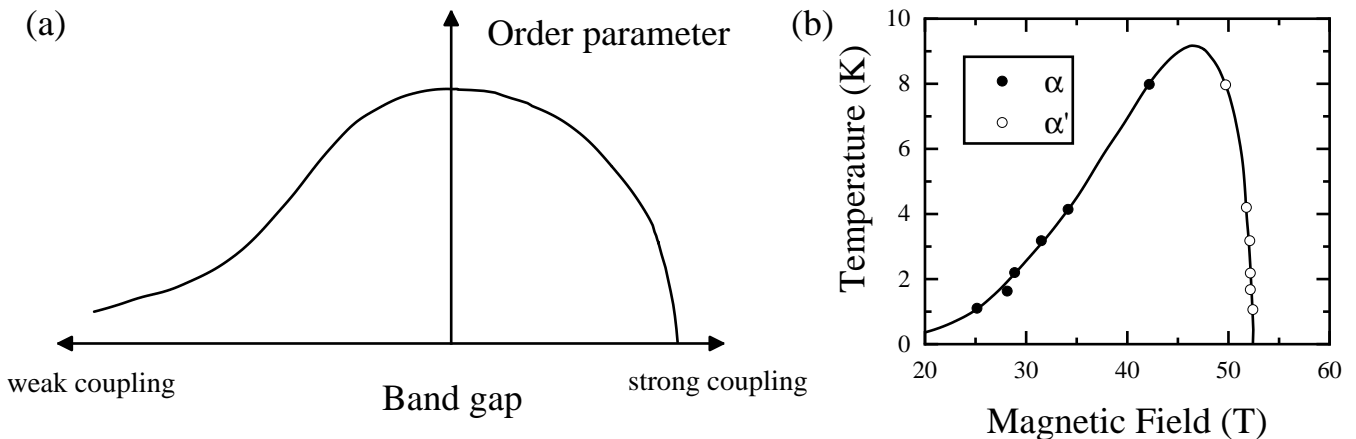


FIG. 1. **Comparing a theoretical and an experimental phase diagram** (a) The theoretical phase diagram for an excitonic insulator showing the evolution of the ordering energy as a function of the band gap [4, 5]. The order parameter is strongest when the band gap is zero. Note the contrast between the evolution of the order parameter on the two sides of the dome. (b) The experimental phase diagram of graphite at high magnetic field [11, 12]. The insulating state resides inside a dome in the (field, temperature) plane. A second dome (starting at ≈ 53 T and ending at ≈ 70 T [15]) is not shown. Note the contrast between the gradual rise of the critical temperature to the summit of the dome and its abrupt drop afterwards.

magnetoexcitonic condensates in heterostructure superconducting graphene [61].

Here, we present a systematic study of the evolution of the phase diagram of graphite and its Fermi surface by measuring the magnetoresistance for $H \parallel c$ -axis up to 60 T under hydrostatic pressure up to 1.7 GPa. We find that both the lower (low-field) and the upper (high-field) boundaries of the first dome shift to higher fields with increasing pressure. In striking contrast, the summit of the dome is insensitive to pressure. Our study of the evolution of the Fermi surface pockets with pressure demonstrates that across the lower boundary, the BCS relation between the critical temperature and the density of states (set by the degeneracy of the Landau levels) remains valid under pressure. This weak-coupling behavior is disrupted at high magnetic field, when the critical temperature approaches a ceiling set by a parameter set by BEC, which shows little variation with pressure.

II. METHODS

The pressure cell used in this study has been developed to fit in the pulsed field magnets of the Wuhan National High Magnetic Field Center. It is Bridgman type pressure cell adapted from the design of D. Braithwaite *et al.* [62]. The cell body, with a diameter of 11.8 mm and a length of 36 mm, is crafted from MP35N (see Fig. 2(a) for a photo of the cell). The anvils are machined of ZrO₂. Daphne 7373 was used as the pressure transmitting medium (see the supplement for additional details regarding the pressure cell). The sample space of diameter 1 mm can host a sample and a tin sample as shown on Fig. 2(b). The superconducting transition temperature of the tin sample is used as an *in-situ* measure-

ment of the pressure in the cell. The magnetoresistance of graphite was measured with the standard four-probe method. The electrical current was applied in-plane and the magnetic field was applied along the c -axis for all samples. Sample temperature has been measured by a calibrated cernox thermometer attach to the body of the pressure cell. The unavoidable heating of the pressure cell during the pulse has been corrected through a comparison of the anomalies position with and without the gasket at ambient pressure (see supplement material section S₁).

III. RESULTS

Fig. 2(c)-(h) shows the field dependence of the in-plane resistivity (ρ_{xx}) at various temperatures for pressures of 0, 0.12, 0.35, 0.72, 1.12 and 1.7 GPa (see the supplement material section S₂ for the Hall response). Curves are shifted for clarity. At zero pressure, see Fig. 2(c), ρ_{xx} displays a sudden increase above 20 T. This jump shifts to higher magnetic field as the temperature increases. Above 10 K, as reported previously [12], the anomaly vanishes. The onset transition and the high field boundary, labelled α and α' , following previous authors [12], are marked by black squares and red circles, respectively. The phase between α and α' is labelled the phase A (the first dome) [16, 17].

Under pressure, α , α' , and therefore the phase A, shift towards higher magnetic fields. The evolution of the T - B phase diagram with pressure is shown in Fig. 3(a)-(f). Above 1.12 GPa, the high-field boundary α' moves above 60 T and exits our range of measurement. In contrast, the summit of the dome remains at 10.2 K unchanged by the pressure, as indicated by the horizontal dashed line.

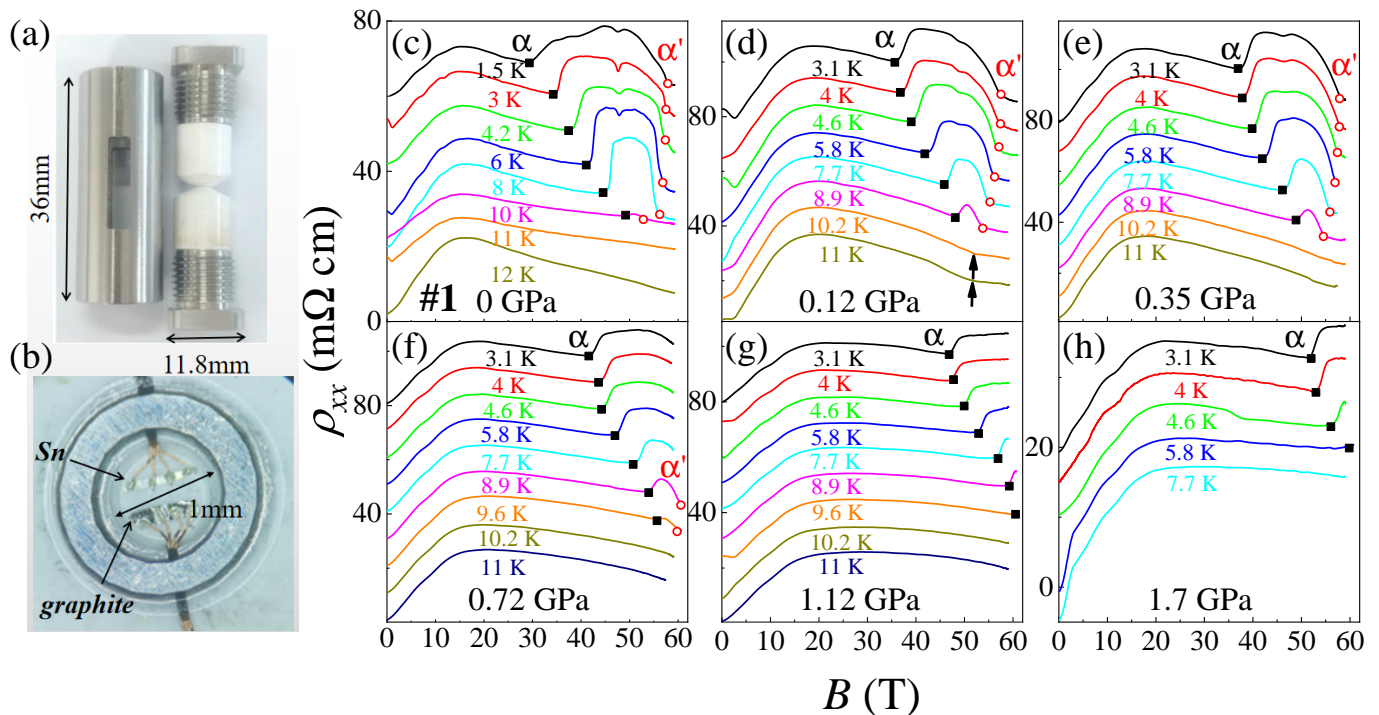


FIG. 2. **Pressure cell and magneto resistivity results :** (a) Photo of the pressure cell of external diameter 11.8 mm used in the pulsed-magnet (b) Photo of a Kish graphite sample in the pressure cell. The pressure was determined in-situ by the superconducting temperature transition of tin. (c)-(h) Field dependence of ρ_{xx} up to 60 T at various temperatures and for different pressures. Curves are shifted for clarity. The onset transition (α) and the re-entrant transition (α') of the first dome are indicated with black solid squares and red empty circles. The Shubnikov-de Haas oscillations at low-field are also observed at low temperatures (see supplemental material S₂). The α and α' are shifting to higher field after applied pressure. Under 1.12 GPa, the α' shifts beyond 60 T.

Black arrows on Fig. 2(d) and solid circles in Fig. 3(b) indicate the kinks in ρ_{xx} which survives above 10 K. A similar anomaly at ambient pressure, above the field induced state, was detected in measurements of the sound velocity [16], the out-of-plane magnetoresistance (ρ_{zz}) [23] and the Nernst effect [18]. This kink marks the field at which electron and hole Landau sub-bands simultaneously cross the Fermi level [18, 23], creating the most favorable conditions for an electronic instability such as an exciton condensation.

IV. DISCUSSION

A. BCS regime under pressure

At ambient pressure, in the low-field boundary of the phase A, the critical temperature (T) and field (B) follows:

$$T(B) = T^* \exp(-B^*/B) \quad (1)$$

where T^* and B^* are adjustable parameters. This formula mimics a BCS-type expression: $k_B T_c(B) = 1.14 E_F \exp(-\frac{1}{N(E_F)V})$, where $N(E_F)$ is the density of

states (DOS) at the Fermi energy (E_F) and V is the pairing interaction [63, 64]. In this framework, T^* is proportional to the Fermi energy, B^* is inversely proportional to the $N(E_F)V$ product. The change of the critical temperature with the magnetic field is due to field dependence of the DOS which increases linearly with the magnetic field, driven by the degeneracy of the Landau levels [19]. With increasing magnetic field, both the DOS and the critical temperature increase and approach the summit of the dome.

Fig. 3(h)-(m) show the evolution of T vs B^{-1} with pressure. For all studied pressures, Eq. 1 is satisfied which allows a determination of T^* and B^* . Fig. 3(g) and (n) show the pressure dependence of T^* and B^* normalized by the ambient pressure values. Both quantities increase linearly with the pressure. Their slope is similar: $a = 0.41 \pm 0.02 \text{ GPa}^{-1}$ for $T^*(P)$ and $a = 0.4 \pm 0.03 \text{ GPa}^{-1}$ for $B^*(P)$.

To quantify the change of the Fermi surface induced by the pressure we studied the evolution of the Shubnikov-de Haas (SdH) oscillations in DC field up to 16 T and 1.7 GPa (see supplementary material section S₃). Fig. 4(a) shows the evolution of the SdH frequencies (F) and the effective mass m^* deduced from their temperature dependence. The normalised pressure dependence of the Fermi

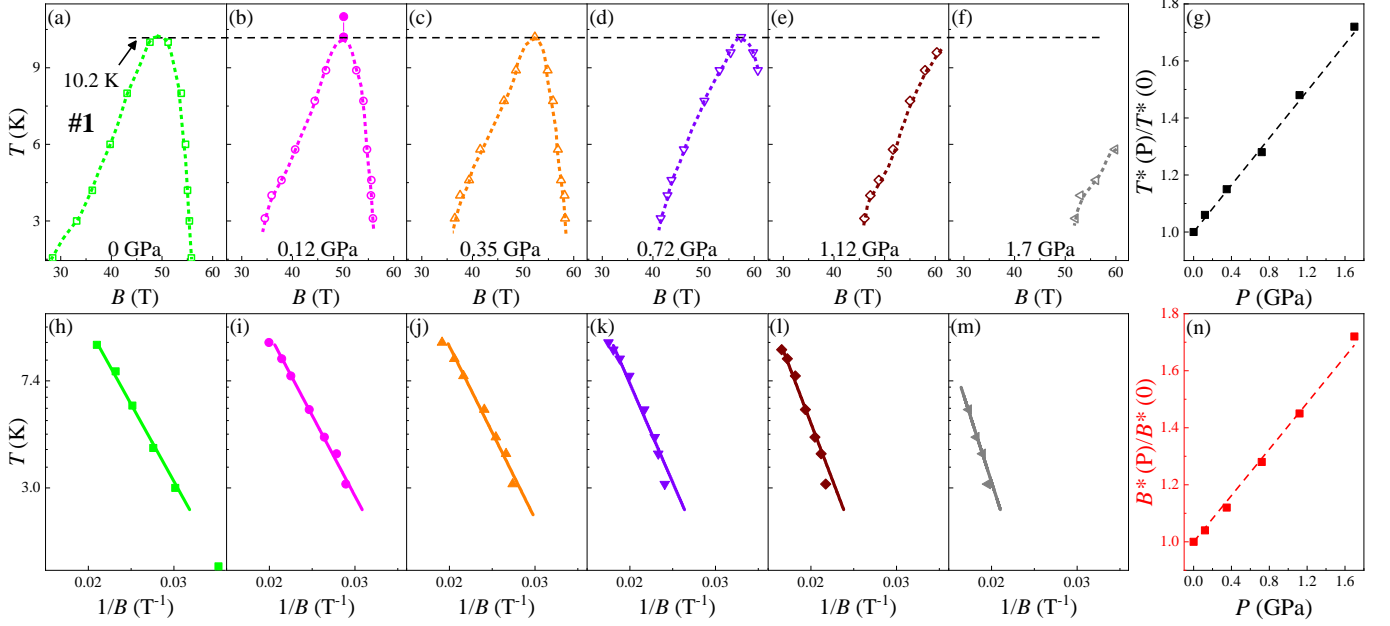


FIG. 3. **$T - B$ phase diagram of graphite under pressure** : (a)-(f) $T - B$ phase diagrams for $H \parallel c$ -axis at the pressure of 0, 0.12, 0.35, 0.72, 1.12 and 1.7 GPa. The dome is shifting to higher field under hydrostatic pressure. In contrast, the summit of the dome is independent of the pressure. The two solid circles in the (b) show the kinks in magnetoresistance. (h)-(m) T vs $1/B$ at different pressure. The solid lines are a fit of the low-field boundary of phase α using Eq.(1), see the text. (g)(n) Pressure dependence of the parameters T^* and B^* deduced from the fits.

	Methods	a (GPa^{-1})
Brandt <i>et al.</i> (1.7 GPa, 2 K)	$\partial \ln m^* / \partial P$	0.43 ± 0.03 [65]
Iye <i>et al.</i> (1.05 GPa, < 1.5 K)	$T^*(P) = (1 + aP)T^*(0)$ $B^*(P) = (1 + aP)B^*(0)$	0.29 ± 0.01 [63] 0.29 ± 0.01 [63]
Present work (1.7 GPa, 3 K-10 K)	$\partial \ln m^* / \partial P$	0.38 ± 0.02
	$T^*(P) = (1 + aP)T^*(0)$	0.41 ± 0.03
	$B^*(P) = (1 + aP)B^*(0)$ $E_F(P) = (1 + aP)E_F(0)$	0.4 ± 0.02 0.38 ± 0.03

TABLE I. Coefficient of the linear pressure dependence of $\partial \ln m^* / \partial P$, T^* , B^* and E_F according to [65, 66] and our study.

energy of electrons ($E_{F,e,\perp}$), holes ($E_{F,h,\perp}$) and their average ($E_{F,ave} = (E_{F,h} + E_{F,e})/2$) are shown in Fig. 4(c). The $\partial \ln m^* / \partial P$ and $E_{F,ave}$ increase linearly with pressure with an slope of $a = 0.38 \pm 0.03 \text{ GPa}^{-1}$, in good agreement with an early and comprehensive quantum oscillation analysis by Brandt ($a = 0.43 \pm 0.03 \text{ GPa}^{-1}$)[65], see the supplementary material section S₄.

Table I summarizes the amplitude of the pressure dependence of the four quantities studied : $T^*(P)$, $B^*(P)$, $E_F(P)$ and $\partial \ln(m^*)/\partial P$ (see the supplemental information S₄). Remarkably they display the same pressure dependence. This striking observation can be linked to the pressure dependence of a single parameter (γ_2) of the Slonczewski-Weiss-McCure (SWM) tight-binding model of the band structure of graphite. This model is formed by seven energy scales (γ_i ; $i = 0 - 5$ and Δ) [67] that represent

interactions between neighboring carbon atoms. The parameter γ_2 quantify the inter-layer coupling between the two sub-lattices. It sets the c -axis dispersion : $E(k_z) = -2\gamma_2 \sin(\frac{c_0 k_z}{2})$ where $c_0 = 2c$ with c is the inter-layer distance and k_z is the c -axis momentum [66]. Under pressure the inter-layer coupling and γ_2 increase linearly with pressure : $\gamma_2(P) = (1 + aP)\gamma_2(0)$ with a ranging from 0.23 to 0.43 GPa^{-1} according to various experiments done at different temperatures [63, 65]. Thus, the pressure impacts T^* , which is approximately proportional to E_F , and B^* , which scales inversely with $N(E_F)V$ if the pairing interaction V does not change significantly. Our findings suggest that the pressure-induced variation in γ_2 is not only the driving force behind the linear increase in E_F , but also in $N(E_F)$ (as detailed in supplemental material S5) [63].

B. BCS-BEC cross-over

In contrast to the low-field boundary regime that is tuned by the pressure, the maximum critical temperature of the dome is independent of it. This result points to two distinct regimes in the dome. It was recently noticed that the summit of the dome at ambient pressure, which occurs at $\simeq 10$ K, is close to the degeneracy temperature of excitons [18]. Indeed the inter-plane distance between excitons and the interplane thermal de Broglie wavelength match each other [18] at this temperature, indicating that this summit corresponds to the BEC temperature. The

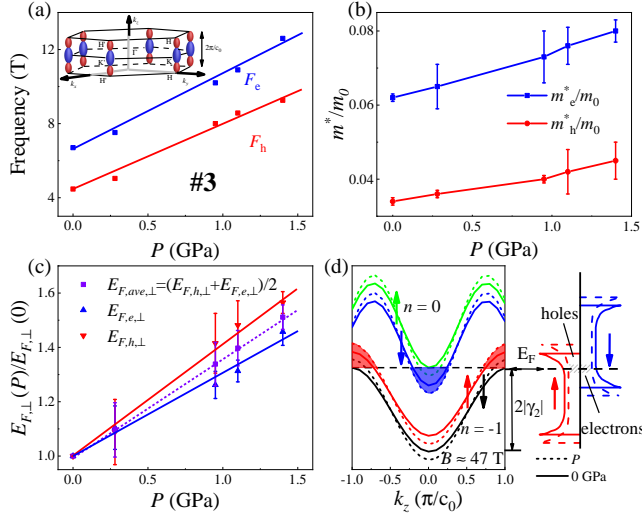


FIG. 4. **Pressure dependence of the Fermi surface properties of graphite:** (a) Pressure dependence of the SdH frequencies (F) of the electrons (blue) and holes (red). Inset : sketch of the Fermi surface of graphite, formed by six adjacent ellipsoid pockets (electron in blue and hole in red). (b) Pressure dependence of the effective masses m of the electrons (blue) and holes (red). (c) Pressure dependence of the Fermi energy of the electrons, holes and its average (purple points). (d) Sketch of the Landau-level spectrum of graphite close to the summing of the dome. The dashed-solid curves represent the conditions at ambient pressure, while the dashed curves correspond to those under pressure. On the right, the corresponding density of states is depicted.

present results imply that this critical temperature does not show any detectable shift with pressure despite the pressure-induced change of the Fermi temperature.

In order to understand why the summit of the dome is independent of the pressure, let us now put it in the context of the crossover between the BCS to BEC regime. In the weak coupling (BCS) limit, the coherence length (ξ) is much longer than the distance between e-h pairs (d), allowing the applicability of a mean-field BCS-type formula linking the critical temperature to the density of states. Graphite being an anisotropic material, both length scales are anisotropic: $d_{\perp} \gg d_{\parallel}$ (the interparticle distances in the basal plane $d_{\perp} = 19.5$ nm [18] and $d_{\parallel} \approx 1$ nm [19]) and $\xi_{\perp} \ll \xi_{\parallel}$. In contrast to d_{\perp} , which depends on carrier concentration, d_{\parallel} is set by the distance between layers. One can also estimate ξ_{\parallel} , the coherence length along the c -axis and compare it with d_{\parallel} in order to see how the system evolves from the weak limit ($\xi_{\parallel} > d_{\parallel}$) to the strong limit ($\xi_{\parallel} \approx d_{\parallel}$).

Fig. 5(a) shows the evolution of ξ_{\parallel} with magnetic field using the BCS formula $\xi_{\parallel} = \frac{\hbar^2 k_{F,\parallel}}{\pi m_{\parallel}^* \Delta_c} = \frac{\hbar v_{F,\parallel}}{\pi \Delta_c}$. Here, Δ_c is the energy gap measured by out-of-plane resistance measurements [9]. It increases with the magnetic field. Assuming $k_{F,\parallel}$ to be $\approx \frac{\pi}{8c}$ [19, 68], allows one to extract ξ_{\parallel} and see that its steady decrease with increasing magnetic field decelerates first and then saturates to $2c$ (in

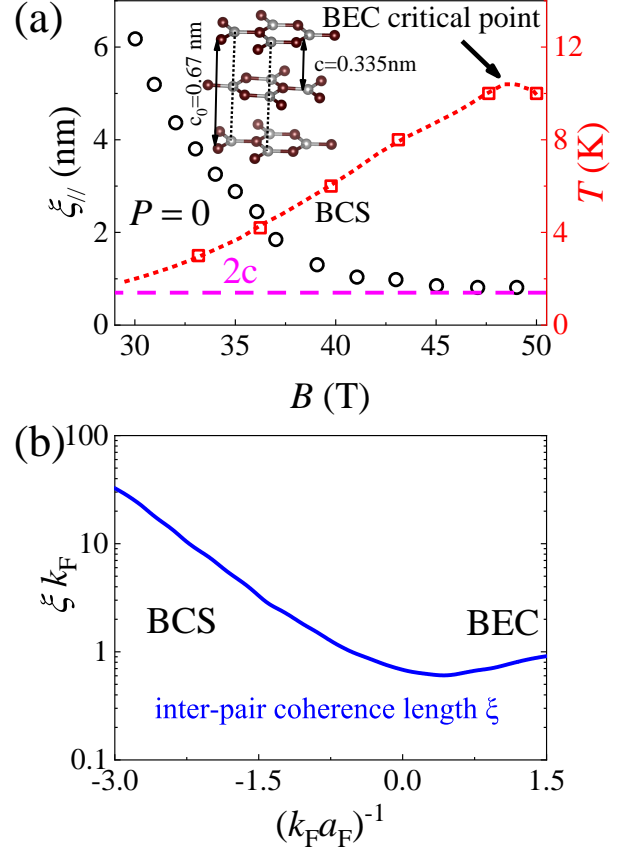


FIG. 5. **BCS-BEC crossover in graphite:** (a) Field dependence of ξ_{\parallel} (black open circle points, see the text for the definition), at ambient pressure compare with the field dependence of the critical temperature (T) in red square points. The purple dashed line is the A-A interlayer distance c_0 . When ξ_{\parallel} saturates to c_0 , T saturates also at its largest value. The inset shows the lattice structure of graphite. (b) The inter-pair coherence length ξk_F (blue full line) at the mean-field level *vs.* the coupling parameter $(k_F a_F)^{-1}$. Reproduced from Ref.[40].

other words, d_{\parallel}). Thus, there is an upper bound to the critical temperature, because the coherence length cannot become shorter than the interbosonic distance. This picture is to be compared with the theoretical picture of the BCS-BEC crossover shown in Fig. 5(b). In the weak-coupling BCS regime [40], the inter-pair coherence length ξ decreases. In the strong-coupling BEC regime, when $(k_F a_F)^{-1} \geq 1$ [40], the interaction increases further, but ξ ceases to decrease. This is consistent with our observation of the decrease in ξ_{\parallel} followed by its saturation. Furthermore, at the BCS-BEC crossover, ξk_F shows a minimum at ≈ 0.6 . In the case of graphite, this corresponds to $\xi = 1.53c$, broadly consistent with the saturation of ξ at $\approx 2c$ found in Fig. 5(a).

How does this picture evolve with pressure? The short answer to the question is that the pressure leaves $2c$ almost unchanged (it changes by less than 3 % at 1 GPa [8]). Since the out-of-plane correlation length cannot be

come shorter than $2c$, the bound to the BCS critical temperature remains identical despite the shift in the parameters. For a more comprehensive answer, one needs to quantify ξ_{\parallel} under pressure. This requires measuring Δ_c . Let us note however, that the change in $v_{F,\parallel}(P)$, inferred from fermiology, is small. It decreases by less than $\approx 10\%$, as a consequence of the decrease in both the effective mass and the Fermi radius (see the supplement material S₃).

In the BCS-BEC crossover, the hierarchy between normalised chemical potential and order parameter change, without altering the ground state and causing any phase transition [69]. The crossover is achieved by changing the ratio of the size of the pairs and the distance between the particles. Therefore, it has been argued [69] that to drive the crossover, one can either change the particle density or the amplitude of the fermion-fermion interaction. The latter road (‘interaction driven’) is taken in the atomic gases with Feshbach resonance [41–48, 69]. The former road ‘density driven’ was theoretically invoked for excitons decades ago [70], but is hard to realize experimentally. Graphite under a strong magnetic field offers an alternative. Our result shows that pairing interaction V is almost pressure independent. It is the increase of DOS, induced by the magnetic field, that drives here the BCS-BEC crossover and not the tuning of the pairing interaction or the particle density.

Lastly, it is noteworthy that valley [10] and orbital [71] degree of freedom can introduce additional complexity in the high magnetic field regime of graphite. Recently, a theoretical study by Kousa, Wei and Macdonald found that the $n = 0$ and $n = 1$ Landau levels of bilayer graphene are sensitive to the details of the particle-hole symmetry breaking and concluded that the mixing of Landau orbitals may affect the physics of bulk graphite at high magnetic fields [72]. The link between two research

fields, field-induced electron-hole pairing in 3D graphite and fractional quantum Hall effect in 2D graphene remains a totally unexplored territory.

V. CONCLUSIONS

In summary, we performed a study of magnetoresistance of Kish graphite up to 60 T under pressure up to 1.7 GPa. The α and α' transitions shift to higher fields, while the summit of the dome remains at the same temperature. We argued that this observation can be understood by considering the BCS parameters of the low field transitions and the BCS-BES crossover constraints at the summit of the dome.

VI. ACKNOWLEDGMENTS

This work was supported by The National Key Research and Development Program of China (Grant No.2022YFA1403500), the National Science Foundation of China (Grant No.12004123, 51861135104 and No.11574097) and the Fundamental Research Funds for the Central Universities (Grant no. 2019kfyXMBZ071). K. B was supported by the Agence Nationale de la Recherche (ANR-19-CE30-0014-04). B. F. was supported by the Agence Nationale de la Recherche (ANR-18-CE92-0020-01) and by Jeunes Equipes de l’Institut de Physique du Collège de France. X. L. acknowledges the China National Postdoctoral Program for Innovative Talents (Grant No.BX20200143) and the China Postdoctoral Science Foundation (Grant No.2020M682386).

* zengwei.zhu@hust.edu.cn

-
- [1] N. F. Mott, The transition to the metallic state, *The Philosophical Magazine: A Journal of Theoretical Experimental and Applied Physics* **6**, 287 (1961).
 - [2] R. S. Knox, Theory of excitons, *Solid State Phys. Suppl.* **5**, 100 (1963).
 - [3] L. Keldysh and A. Kozlov, The metal-dielectric divalent crystal phase transition, *Sov. Phys. JETP* **27**, 521 (1967).
 - [4] A. Kozlov and L. Maksimov, The metal-dielectric divalent crystal phase transition, *Sov. Phys. JETP* **21**, 790 (1965).
 - [5] D. Jérôme, T. M. Rice, and W. Kohn, Excitonic insulator, *Phys. Rev.* **158**, 462 (1967).
 - [6] A. Abrikosov, On the phase diagram of an excitonic insulator in a strong magnetic field, *Sov. Phys. JETP* **38**, 750 (1974).
 - [7] P. Nozières and S. Schmitt-Rink, Bose condensation in an attractive fermion gas: From weak to strong coupling superconductivity, *J. Low Temp. Phys.* **59**, 195 (1985).
 - [8] N. Brandt, S. Chudinov, and Y. G. Ponomarev, Modern problems in condensed matter sciences, Agranovich and AA Maradudin: North-Holland, Amsterdam **20** (1988).
 - [9] B. Fauqué and K. Behnia, Phase transitions induced by a magnetic field in graphite, in *Basic Physics of Functionalized Graphite*, edited by P. D. Esquinazi (Springer International Publishing, Cham, 2016) pp. 77–96.
 - [10] D. Yoshioka and H. Fukuyama, Electronic phase transition of graphite in a strong magnetic field, *J. Phys. Soc. Jpn.* **50**, 725 (1981).
 - [11] H. Yaguchi and J. Singleton, Destruction of the field-induced density-wave state in graphite by large magnetic fields, *Phys. Rev. Lett.* **81**, 5193 (1998).
 - [12] H. Yaguchi and J. Singleton, A high-magnetic-field-induced density-wave state in graphite, *J. Phys.: Condens. Matter* **21**, 344207 (2009).
 - [13] B. Fauqué, Z. Zhu, T. Murphy, and K. Behnia, Nernst response of the Landau tubes in graphite across the quantum limit, *Phys. Rev. Lett.* **106**, 246405 (2011).
 - [14] K. Akiba, A. Miyake, H. Yaguchi, A. Matsuo, K. Kindo, and M. Tokunaga, Possible excitonic phase of graphite in the quantum limit state, *J. Phys. Soc. Jpn.* **84**, 054709

- (2015).
- [15] B. Fauqué, D. LeBoeuf, B. Vignolle, M. Nardone, C. Proust, and K. Behnia, Two phase transitions induced by a magnetic field in graphite, *Phys. Rev. Lett.* **110**, 266601 (2013).
- [16] D. LeBoeuf, C. W. Rischau, G. Seyfarth, R. Küchler, M. Berben, S. Wiedmann, W. Tabis, M. Frachet, K. Behnia, and B. Fauqué, Thermodynamic signatures of the field-induced states of graphite, *Nat. Commun.* **8**, 1337 (2017).
- [17] Z. Zhu, P. Nie, B. Fauqué, B. Vignolle, C. Proust, R. D. McDonald, N. Harrison, and K. Behnia, Graphite in 90 T: Evidence for strong-coupling excitonic pairing, *Phys. Rev. X* **9**, 011058 (2019).
- [18] J. Wang, P. Nie, X. Li, H. Zuo, B. Fauqué, Z. Zhu, and K. Behnia, Critical point for Bose-Einstein condensation of excitons in graphite, *Proc. Natl. Acad. Sci.* **117**, 30215 (2020).
- [19] C. Marcenat, T. Klein, D. LeBoeuf, A. Jaoui, G. Seyfarth, J. Kačmarčík, Y. Kohama, H. Cercellier, H. Aubin, K. Behnia, and B. Fauqué, Wide critical fluctuations of the field-induced phase transition in graphite, *Phys. Rev. Lett.* **126**, 106801 (2021).
- [20] S. Tanuma, R. Inada, A. Furukawa, O. Takahashi, Y. Iye, and Y. Onuki, Physics in high magnetic fields, Springer Series in Solid State Sciences (1981).
- [21] Z. Zhu, H. Yang, B. Fauqué, Y. Kopelevich, and K. Behnia, Nernst effect and dimensionality in the quantum limit, *Nat. Phys.* **6**, 26 (2010).
- [22] J. M. Schneider, B. A. Piot, I. Sheikin, and D. K. Maude, Using the de Haas–van Alphen effect to map out the closed three-dimensional Fermi surface of natural graphite, *Phys. Rev. Lett.* **108**, 117401 (2012).
- [23] Z. Zhu, R. D. McDonald, A. Shekhter, B. J. Ramshaw, K. A. Modic, F. F. Balakirev, and N. Harrison, Magnetic field tuning of an excitonic insulator between the weak and strong coupling regimes in quantum limit graphite, *Sci. Rep.* **7**, 1733 (2017).
- [24] I. F. Silvera, Bose-Einstein condensation, *Am. J. Phys.* **65**, 570 (1997).
- [25] N. P. Wilson, W. Yao, J. Shan, and X. Xu, Excitons and emergent quantum phenomena in stacked 2D semiconductors, *Nature* **599**, 383 (2021).
- [26] Z. Wang, D. A. Rhodes, K. Watanabe, T. Taniguchi, J. C. Hone, J. Shan, and K. F. Mak, Evidence of high-temperature exciton condensation in two-dimensional atomic double layers, *Nature* **574**, 76 (2019).
- [27] J. I. A. Li, T. Taniguchi, K. Watanabe, J. Hone, and C. R. Dean, Excitonic superfluid phase in double bilayer graphene, *Nat. Phys.* **13**, 751 (2017).
- [28] L. V. Butov, Cold exciton gases in coupled quantum well structures, *J. Phys.: Condens. Matter* **19**, 295202 (2007).
- [29] X. Liu, K. Watanabe, T. Taniguchi, B. I. Halperin, and P. Kim, Quantum hall drag of exciton condensate in graphene, *Nat. Phys.* **13**, 746 (2017).
- [30] A. Kogar, M. S. Rak, S. Vig, A. A. Husain, F. Flicker, Y. I. Joe, L. Venema, G. J. MacDougall, T. C. Chiang, E. Fradkin, J. van Wezel, and P. Abbamonte, Signatures of exciton condensation in a transition metal dichalcogenide, *Science* **358**, 1314 (2017).
- [31] Y. F. Lu, H. Kono, T. I. Larkin, A. W. Rost, T. Takayama, A. V. Boris, B. Keimer, and H. Takagi, Zero-gap semiconductor to excitonic insulator transition in Ta_2NiSe_5 , *Nat. Commun.* **8**, 14408 (2017).
- [32] J. Klaers, J. Schmitt, F. Vewinger, and M. Weitz, Bose–Einstein condensation of photons in an optical microcavity, *Nature* **468**, 545 (2010).
- [33] J. Bloch, I. Carusotto, and M. Wouters, Non-equilibrium Bose–Einstein condensation in photonic systems, *Nat. Rev. Phys.* **4**, 470 (2022).
- [34] H. Deng, H. Haug, and Y. Yamamoto, Exciton-polariton Bose–Einstein condensation, *Rev. Mod. Phys.* **82**, 1489 (2010).
- [35] J. Kasprzak, M. Richard, S. Kundermann, A. Baas, P. Jeambrun, J. M. J. Keeling, F. M. Marchetti, M. H. Szymańska, R. André, J. L. Staehli, V. Savona, P. B. Littlewood, B. Deveaud, and L. S. Dang, Bose-Einstein condensation of exciton polaritons, *Nature* **443**, 409 (2006).
- [36] V. Zapf, M. Jaime, and C. D. Batista, Bose-Einstein condensation in quantum magnets, *Rev. Mod. Phys.* **86**, 563 (2014).
- [37] S. O. Demokritov, V. E. Demidov, O. Dzyapko, G. A. Melkov, A. A. Serga, B. Hillebrands, and A. N. Slavin, Bose–Einstein condensation of quasi-equilibrium magnons at room temperature under pumping, *Nature* **443**, 430 (2006).
- [38] T. Giamarchi, C. Rüegg, and O. Tchernyshyov, Bose–Einstein condensation in magnetic insulators, *Nat. Phys.* **4**, 198 (2008).
- [39] Q. Chen, J. Stajic, S. Tan, and K. Levin, Bcs–bec crossover: From high temperature superconductors to ultracold superfluids, *Phys. Rep.* **412**, 1 (2005).
- [40] G. C. Strinati, P. Pieri, G. Röpke, P. Schuck, and M. Urban, The BCS-BEC crossover: From ultra-cold Fermi gases to nuclear systems, *Phys. Rep.* **738**, 1 (2018).
- [41] S. Jochim, M. Bartenstein, A. Altmeyer, G. Hendl, S. Riedl, C. Chin, J. Hecker Denschlag, and R. Grimm, Bose-Einstein condensation of molecules, *Science* **302**, 2101 (2003).
- [42] M. Greiner, C. A. Regal, and D. S. Jin, Emergence of a molecular Bose-Einstein condensate from a Fermi gas, *Nature* **426**, 537 (2003).
- [43] M. W. Zwierlein, C. A. Stan, C. H. Schunck, S. M. F. Raupach, S. Gupta, Z. Hadzibabic, and W. Ketterle, Observation of Bose-Einstein condensation of molecules, *Phys. Rev. Lett.* **91**, 250401 (2003).
- [44] C. A. Regal, M. Greiner, and D. S. Jin, Observation of resonance condensation of fermionic atom pairs, *Phys. Rev. Lett.* **92**, 040403 (2004).
- [45] J. Kinast, S. L. Hemmer, M. E. Gehm, A. Turlapov, and J. E. Thomas, Evidence for superfluidity in a resonantly interacting Fermi gas, *Phys. Rev. Lett.* **92**, 150402 (2004).
- [46] T. Bourdel, L. Khaykovich, J. Cubizolles, J. Zhang, F. Chevy, M. Teichmann, L. Tarruell, S. J. J. M. F. Kokkelmans, and C. Salomon, Experimental study of the BEC-BCS crossover region in lithium 6, *Phys. Rev. Lett.* **93**, 050401 (2004).
- [47] M. W. Zwierlein, C. A. Stan, C. H. Schunck, S. M. F. Raupach, A. J. Kerman, and W. Ketterle, Condensation of pairs of fermionic atoms near a feshbach resonance, *Phys. Rev. Lett.* **92**, 120403 (2004).
- [48] M. Bartenstein, A. Altmeyer, S. Riedl, S. Jochim, C. Chin, J. H. Denschlag, and R. Grimm, Crossover from a molecular Bose-Einstein condensate to a degenerate Fermi gas, *Phys. Rev. Lett.* **92**, 120401 (2004).
- [49] Y. Suzuki, K. Wakamatsu, J. Ibuka, H. Oike, T. Fujii, K. Miyagawa, H. Taniguchi, and K. Kanoda, Mott-driven

- BEC-BCS crossover in a doped spin liquid candidate κ -(BEDT-TTF)₄Hg_{2.89}Br₈, *Phys. Rev. X* **12**, 011016 (2022).
- [50] R. H. McKenzie, Similarities between organic and cuprate superconductors, *Science* **278**, 820 (1997).
- [51] B. L. Kang, M. Z. Shi, S. J. Li, H. H. Wang, Q. Zhang, D. Zhao, J. Li, D. W. Song, L. X. Zheng, L. P. Nie, T. Wu, and X. H. Chen, Preformed cooper pairs in layered FeSe-based superconductors, *Phys. Rev. Lett.* **125**, 097003 (2020).
- [52] B. D. Faeth, S.-L. Yang, J. K. Kawasaki, J. N. Nelson, P. Mishra, C. T. Parzyck, C. Li, D. G. Schlom, and K. M. Shen, Incoherent cooper pairing and pseudogap behavior in single-layer FeSe/SrTiO₃, *Phys. Rev. X* **11**, 021054 (2021).
- [53] Y. Saito, T. Nojima, and Y. Iwasa, Highly crystalline 2D superconductors, *Nat. Rev. Mater.* **2**, 16094 (2016).
- [54] Y. Nakagawa, Y. Kasahara, T. Nomoto, R. Arita, T. Nojima, and Y. Iwasa, Gate-controlled BCS-BEC crossover in a two-dimensional superconductor, *Science* **372**, 190 (2021).
- [55] C. Richter, H. Boschker, W. Dietsche, E. Fillis-Tsirakis, R. Jany, F. Loder, L. F. Kourkoutis, D. A. Muller, J. R. Kirtley, C. W. Schneider, and J. Mannhart, Interface superconductor with gap behaviour like a high-temperature superconductor, *Nature* **502**, 528 (2013).
- [56] I. Božović and J. Levy, Pre-formed cooper pairs in copper oxides and LaAlO₃-SrTiO₃ heterostructures, *Nat. Phys.* **16**, 712 (2020).
- [57] M. Oh, K. P. Nuckolls, D. Wong, R. L. Lee, X. Liu, K. Watanabe, T. Taniguchi, and A. Yazdani, Evidence for unconventional superconductivity in twisted bilayer graphene, *Nature* **600**, 240 (2021).
- [58] Y. Cao, V. Fatemi, S. Fang, K. Watanabe, T. Taniguchi, E. Kaxiras, and P. Jarillo-Herrero, Unconventional superconductivity in magic-angle graphene superlattices, *Nature* **556**, 43 (2018).
- [59] H. Kim, Y. Choi, C. Lewandowski, A. Thomson, Y. Zhang, R. Polski, K. Watanabe, T. Taniguchi, J. Alicea, and S. Nadj-Perge, Evidence for unconventional superconductivity in twisted trilayer graphene, *Nature* **606**, 494 (2022).
- [60] J. M. Park, Y. Cao, K. Watanabe, T. Taniguchi, and P. Jarillo-Herrero, Tunable strongly coupled superconductivity in magic-angle twisted trilayer graphene, *Nature* **590**, 249 (2021).
- [61] X. Liu, J. I. A. Li, K. Watanabe, T. Taniguchi, J. Hone, B. I. Halperin, P. Kim, and C. R. Dean, Crossover between strongly coupled and weakly coupled exciton superfluids, *Science* **375**, 205 (2022).
- [62] D. Braithwaite, W. Knafo, R. Settai, D. Aoki, S. Kurahashi, and J. Flouquet, Pressure cell for transport measurements under high pressure and low temperature in pulsed magnetic fields, *Rev. Sci. Instrum.* **87**, 023907 (2016).
- [63] Y. Iye, C. Murayama, N. Mōri, S. Yomo, J. T. Nicholls, and G. Dresselhaus, Effect of pressure on the high-magnetic-field electronic phase transition in graphite, *Phys. Rev. B* **41**, 3249 (1990).
- [64] H. Yaguchi, Y. Iye, T. Takamasu, and N. Miura, Magnetic-field-induced electronic phase transition in graphite. Pulse field experiment at ³He temperatures, *Phys. B Condensed Matter* **184**, 332 (1993).
- [65] N. B. Brandt, A. S. Kotosonov, S. V. Kuvshinnikov, and M. V. Semenov, Effect of pressure on the parameters of the energy spectrum of graphite, *Zh. Eksp. Teor. Fiz* **79**, 946 (1980).
- [66] Y. Iye, P. M. Tedrow, G. Timp, M. Shayegan, M. S. Dresselhaus, G. Dresselhaus, A. Furukawa, and S. Tanuma, High-magnetic-field electronic phase transition in graphite observed by magnetoresistance anomaly, *Phys. Rev. B* **25**, 5478 (1982).
- [67] J. W. McClure, Band structure of graphite and de haas-van alphen effect, *Phys. Rev.* **108**, 612 (1957).
- [68] F. Arnold, A. Isidori, E. Kampert, B. Yager, M. Eschrig, and J. Saunders, Charge density waves in graphite: Towards the magnetic ultraquantum limit, *Phys. Rev. Lett.* **119**, 136601 (2017).
- [69] M. M. Parish, The BCS-BEC crossover, in *Quantum Gas Experiments* (IMPERIAL COLLEGE PRESS, 2014) Chap. 9, pp. 179–197.
- [70] C. Comte and P. Nozières, Exciton Bose condensation: the ground state of an electron-hole gas-I. mean field description of a simplified model, *J. Phys.* **43**, 1069 (1982).
- [71] Y. H. Ho, J. Wang, Y. H. Chiu, M. F. Lin, and W. P. Su, Characterization of landau subbands in graphite: A tight-binding study, *Phys. Rev. B* **83**, 121201 (2011).
- [72] B. M. Kousa, N. Wei, and A. H. MacDonald, Orbital competition in bilayer graphene’s fractional quantum hall effect (2024), [arXiv:2402.10440](https://arxiv.org/abs/2402.10440).

Supplemental Materials for "Tuning the BCS-BEC crossover of electron-hole pairing with pressure"

S1. TEMPERATURE CALIBRATION AND DATA REPRODUCIBILITY

As described in Method, the pressure cell is made of MP35N which has a low thermal conductivity. Yet, during the magnetic field pulse the cell heats due to the unavoidable induced eddy currents. To minimise their effects we show in this manuscript the data collected during the rising field.

To calibrate the change of the temperature induced by the pressure cell on the samples, we utilize the critical field of α in graphite, that is an extremely sensitive *in-situ* thermometers ($\frac{dT_c}{dB} = \frac{T_c B^2}{B^2} \approx 0.2$ K/T @($T = 1.5$ K)). We conducted measurements of ρ_{xx} in the pressure cell, at ambient pressure and up to 60 T, both with and without the gasket in the same sample #1, see Fig. S1(a) and (b). Notably, the gasket is the primary source of heating.

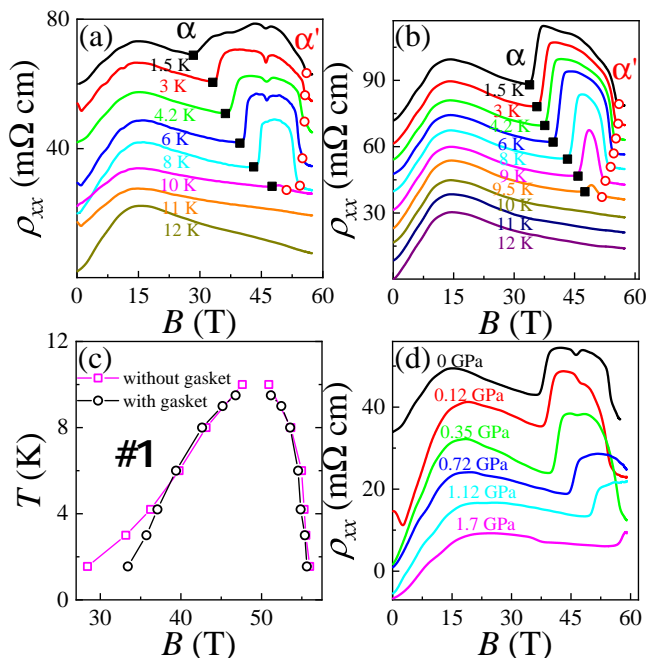


FIG. S1. **Temperature calibration** (a) and (b) The field dependence of the in-plane magneto-resistance (ρ_{xx}) at different temperatures for $B \parallel c$ -axis with gasket or without gasket at 0 GPa in the same sample #1. Data are shifted for clarity. (c) The T - B phase diagrams for $B \parallel c$ -axis with gasket or without gasket at 0 GPa. (d) The magnetic field dependence of resistivity at 4.2 K with different pressure.

The deduced T - B phase diagram with and without the gasket is shown in Fig. S1(c). Below 6 K the measurements with the gasket is clearly at a higher temperature than without. We therefore adjust the temperature ob-

with gasket (K)	1.5	3	4.2	6	8	9	9.5	10
without gasket (K)	3.1	4	4.6	5.8	7.7	8.9	9.6	10.2

TABLE S1. The different temperatures with gasket or without gasket. The temperature in the measurement with gasket under pressure should be to be corrected to the temperature in the measurement without gasket.

tained with the gasket under pressure to align with those taken without the gasket. The corrected temperature values are summarized in Table S1. The data shown in the main text have been collected on sample #1. Measurements of ρ_{xx} in an other sample, labelled #4, are shown on Fig.S2(a)-(e). The pressure of the T - B phase diagram is in excellent agreement with sample #1, see Fig.S2(f)-(j), which demonstrate the reproducibility of the results.

S2. HALL MEASUREMENT UNDER PULSED-MAGNETIC-FIELD

In addition to ρ_{xx} , Hall resistivity (ρ_{xy}) have been measured up to 60 T at various temperatures and for pressure $P = 0, 0.3, 0.75, 0.95$ and 1.6 GPa in the sample #2. In order to extract ρ_{xy} measurements of the transverse voltages have been done for positive and negative magnetic field followed by an anti-symmetrisation.

Fig. S3(a)-(e) shows the field dependence of ρ_{xy} under these pressure. The overall amplitude of ρ_{xy} decreases as the pressure increase due to the increase in the carrier density confirmed by quantum oscillations measurements, see next section. Like in ρ_{xx} , the entrance (and re-entrance) of the field induced state is marked by a sharp increase (decrease) in ρ_{xy} that shift to higher magnetic field once the temperature or the pressure increase. Fig. S3(f)-(i) show the T - B phase diagrams deduced from ρ_{xy} in sample #2 compare with to the one deduced from ρ_{xx} in sample #1. Both type of measurements provide the same results. We note that the summit of the dome remains unchanged and consistent among all the samples studied.

S3. THE SHUBNIKOV-DE HAAS EFFECT AND HALL EFFECT ANALYSE IN LOW-FIELD

a. Analyse of SdH oscillations In order to quantify the change of the Fermi surface as function of the pressure (P), we measured the field dependence of ρ_{xx} and ρ_{xy} of graphite in DC fields with PPMS (Physical Property Measurement System) and Oxford Instrument Integra 16 T system at $P = 0, 0.28, 0.95, 1.1$ and 1.4 GPa, see Fig. S4(a)-(e). On top of a monotonous large magneto-resistance quantum oscillations in ρ_{xx} , known as the Shubnikov-de Haas (SdH) effect, are observed. Study of these oscillations allow to quantify the change of the Fermi surface (effective masses and frequencies)

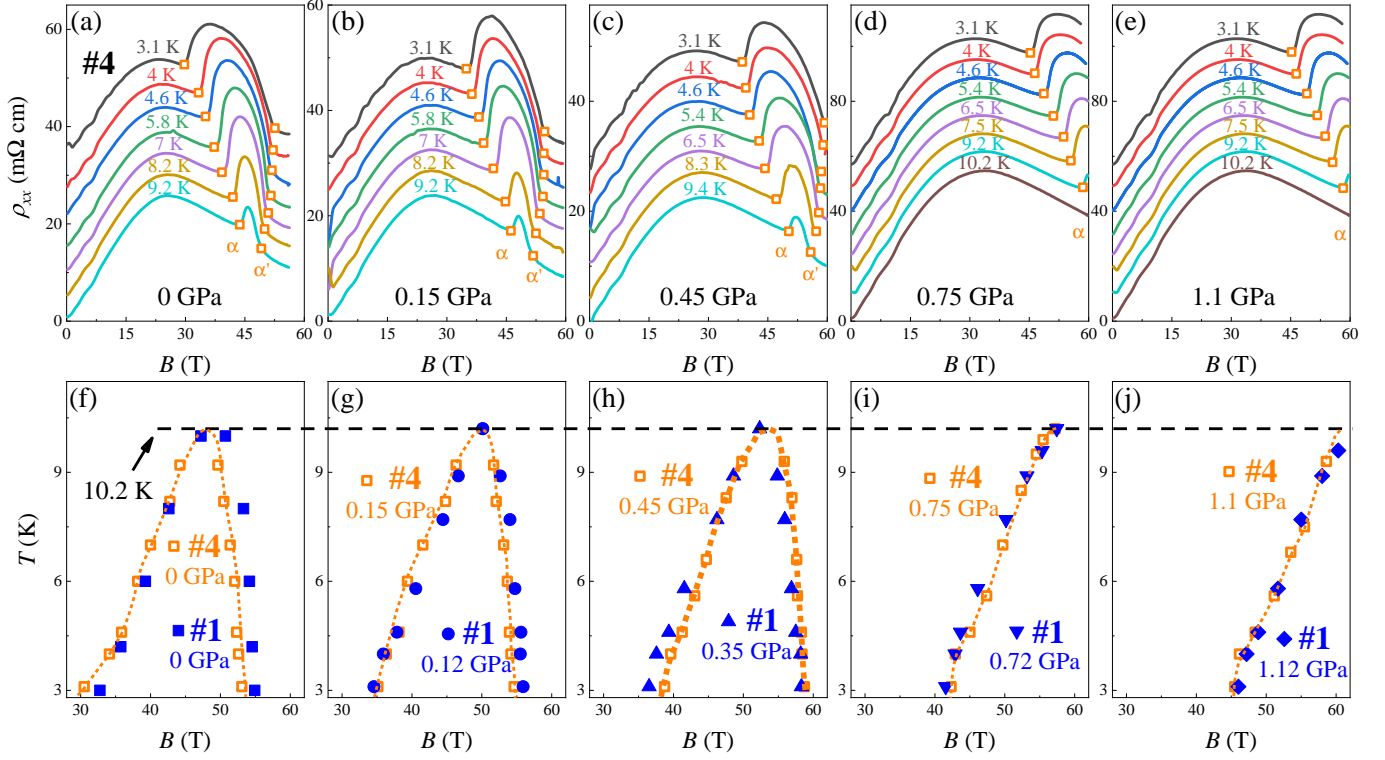


FIG. S2. **T - B phase diagram for the sample #4** (a)-(e) The field dependence of ρ_{xx} at various temperatures up to 60 T for different pressures for sample #4. Curves are shifted for clarity. (f)-(j) The T - B phase diagrams for sample #4 (open orange symbols) for five pressures compared with sample #1 (closed blue symbols).

with the pressure. The trace of these oscillations are clearly visible in the second derivative of ρ_{xx} , see Fig. S4(f)-(j). Fig. S4(k)-(o) show the Landau fan diagram in different pressures, derived from the second derivative of the resistivity ρ_{xx} with respect to the magnetic field squared, $d^2\rho_{xx}/dB^2$, as presented in Fig. S4(f)-(j). At zero pressure, the frequencies of the quantum oscillations, obtained from the slope of Landau fan diagram, are in good agreement with the one reported for the hole and electron pockets, 4.6 T and 6.5 T [1] respectively. Likewise, under pressure, the frequencies of quantum oscillations are also in good agreement with early reports [2].

Quantum oscillations allows also to extract the effective mass of electrons and holes by fitting the temperature dependence of the oscillation amplitude with the thermal damping term $\Delta R_{xx} = (14.69m^*T/B)/\sinh(14.69m^*T/B)$ by using the Lifshitz-Kosevich (L-K) formula [3], where m^* is the effective cyclotron mass. The deduced pressure dependence of the frequencies and masses are shown in Fig. 4 (a) and (b) of the main manuscript.

b. Hall effect As the pressure increases the carrier density increases according to quantum oscillations study. It can also be verified by fitting the Hall effect in low field with the two-band model:

$$\rho_{xy}(B) = \frac{B}{e} \frac{(n_h\mu_h^2 - n_e\mu_e^2) + (n_h - n_e)(\mu_e\mu_h B)^2}{(n_h\mu_h + n_e\mu_e)^2 + (n_h - n_e)^2(\mu_e\mu_h B)^2} \quad (\text{S1})$$

where $n_{e,h}$ and $\mu_{e,h}$ are the electron and hole carrier density and mobility. Fig. S5(e) shows the results of the fit of ρ_{xy} using Eq. S1. Fig. S5(c) and (d) shows the deduced pressure dependence of $n_{e,h}$ and $\mu_{e,h}$. At ambient pressure $n_e = 2.95 \times 10^{18} \text{ cm}^{-3}$ and $n_h = 2.8 \times 10^{18} \text{ cm}^{-3}$, which are consistent with the previous reports [4-6]. The values of $n_{e,h}$ and $\mu_{e,h}$ are also in agreement with the residual resistivity at zero magnetic field $\rho_{xx}(0) = \frac{1}{e} \frac{1}{n_e\mu_e + n_h\mu_h}$. The observed decrease of the mobility of carriers with pressure generally also agrees with the increase in Dingle temperature in graphite under pressure, see [2, 6].

c. Pressure dependence of $v_{F,\parallel}$ The combination of the pressure dependence of the quantum oscillations, the in-planes masses and the carrier densities allows us to estimate the change of the Fermi velocity along the magnetic field ($v_{F,\parallel}$) with the pressure.

Frequencies of quantum oscillations allow an accurate determination of $(k_{F,\perp})$ while the carrier density $n(P) = \bar{k}_F^3(P)/3\pi^2$ where $\bar{k}_F(P) = (k_{F,\perp}^2(P)k_{F,\parallel}(P))^{1/3}$ which allow to determine $k_{F,\parallel}(P)$, the Fermi momentum along the c -axis. Assuming that the rate of change in mass under pressure remains constant but should reverse

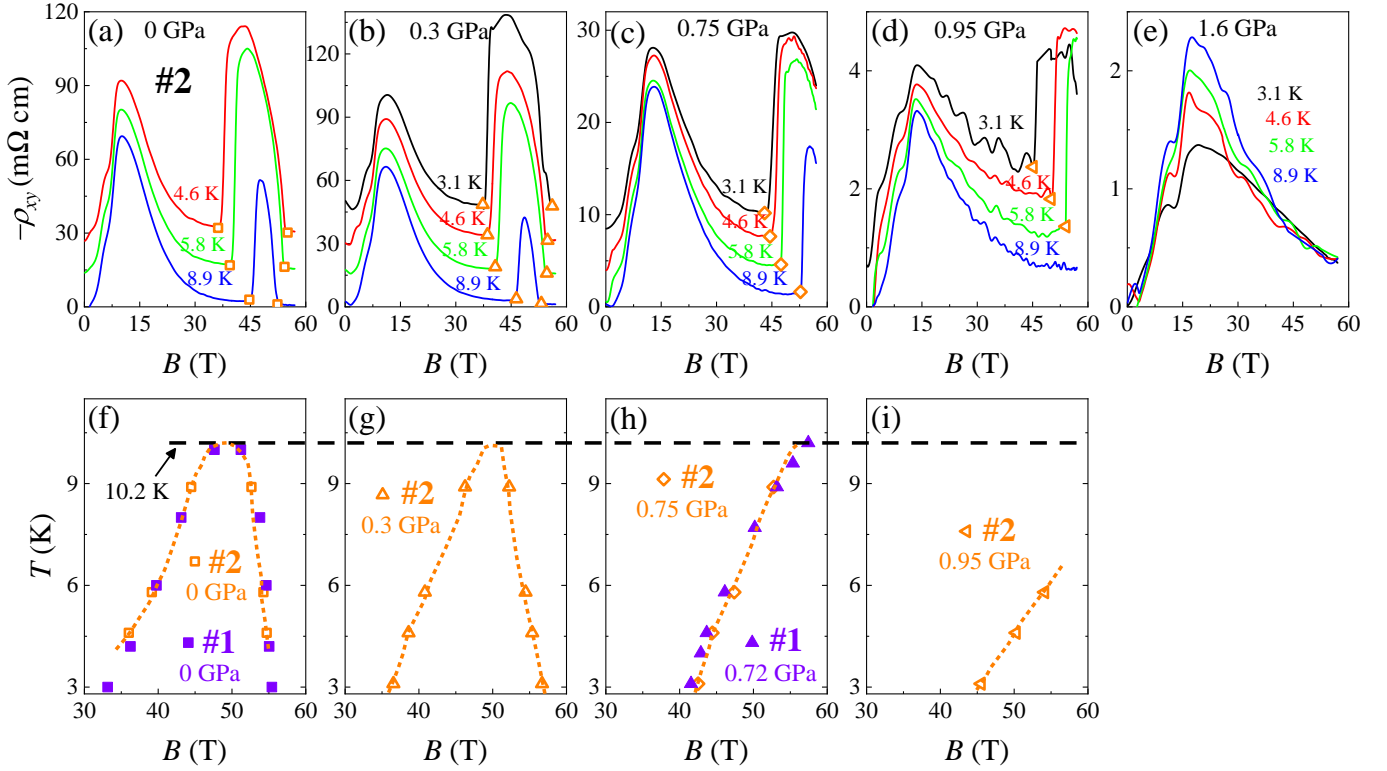


FIG. S3. **The Hall effect under pulsed-magnetic-field** (a)-(e) The in-plane longitudinal Hall resistance at different temperature comprised between 3.1 K to 8.9 K up to 60 T under pressure up to 1.6 GPa. (f)-(i) The T - B phase diagrams for $H \parallel c$ -axis under different pressure from the Hall resistivity of #2 (open orange symbols), and compared with the sample #1 (closed purple symbols).

its direction between the plane and the c -axis ($\frac{m_{\parallel}^*(P)}{m_{\parallel}^*(0)} = \frac{m_{\perp}^*(0)}{m_{\perp}^*(P)}$), we can then estimate $v_{F,\parallel}(P) = \frac{\hbar k_{F,\parallel}(P)}{m_{\parallel}^*(P)}$. Fig. S6 shows the pressure dependence of $v_{F,\parallel}$ for the hole and electron. They only decrease by about less than 10%.

S4. COMPARISON OF THE SWM-MODEL WITH THE QUANTUM OSCILLATIONS FREQUENCIES

The effective masses (m^*) and the extremal cross sections of the Fermi surface in the plane perpendicular to the c -axis are respectively described by the following formulas in the Slonczewski-Weiss-McClure (SWM) model[2]:

$$m_e^*(\Psi) = \frac{4}{3} \left(\frac{\hbar}{a_0} \right)^2 \frac{\gamma_1}{\gamma_0^2} \cos\Psi / \left(1 + \frac{4\gamma_4}{\gamma_0} \cos\Psi \right) \quad (\text{S2})$$

$$m_h^*(\Psi) = \frac{4}{3} \left(\frac{\hbar}{a_0} \right)^2 \frac{\gamma_1}{\gamma_0^2} \cos\Psi / \left(1 - \frac{4\gamma_4}{\gamma_0} \cos\Psi \right) \quad (\text{S3})$$

$$S_e = \frac{3\pi\hbar^2}{4\gamma_0^2 a_0^2} \frac{2\gamma_2 - \varepsilon_F}{(1 + 2\gamma_4/\gamma_0)^2} (\Delta - 2\gamma_1 + 2\gamma_5 + \varepsilon_F) \quad (\text{S4})$$

$$S_h = \frac{3\pi\hbar^2}{4\gamma_0^2 a_0^2} \frac{2\gamma_2 \cos^2\Psi_0 - \varepsilon_F}{(1 - 2\gamma_4 \cos\Psi_0/\gamma_0)^2} (\Delta + 2\gamma_1 \cos\Psi_0 + 2\gamma_5 \cos^2\Psi_0 - \varepsilon_F) \quad (\text{S5})$$

$$S_m = \frac{3\pi\hbar^2}{4\gamma_0^2 a_0^2} \varepsilon_F (\varepsilon_F - \Delta) \quad (\text{S6})$$

where $\Psi = k_z c_0/2$, $c_0 = 2c = 6.7\text{\AA}$, c is the inter-plane distance, $a_0 = 2a = 2.462\text{\AA}$, m_e^* (m_h^*) is the effective mass of the electron (hole). S_e (S_h) is the extremal cross sections of the electron (hole). ε_F is the Fermi energy, $\Delta = \gamma_6$, $\cos\Psi_0 \approx |\varepsilon_F/6\gamma_2|^{1/2}$. S_m is the maximum section of the Fermi surface of the electron. The values of the parameters γ_i ($i = 0 - 5$) (see the Fig. S7), Δ and ε_F , (in eV) are given in Table S3.

Next, we calculate their pressure variation by taking the logarithmic derivatives of S5 and S4 :

$$2.232 \frac{\partial \ln|\gamma_2|}{\partial P} - 1.23 \frac{\partial \ln|\varepsilon_F|}{\partial P} - 0.03 \frac{\partial \ln|\Delta|}{\partial P} + 1.03 \frac{\partial \ln\gamma_1}{\partial P} - 0.026 \frac{\partial \ln|\gamma_5|}{\partial P} - 0.152 \frac{\partial \ln\gamma_4}{\partial P} = \frac{\partial \ln S_e}{\partial P} \quad (\text{S7})$$

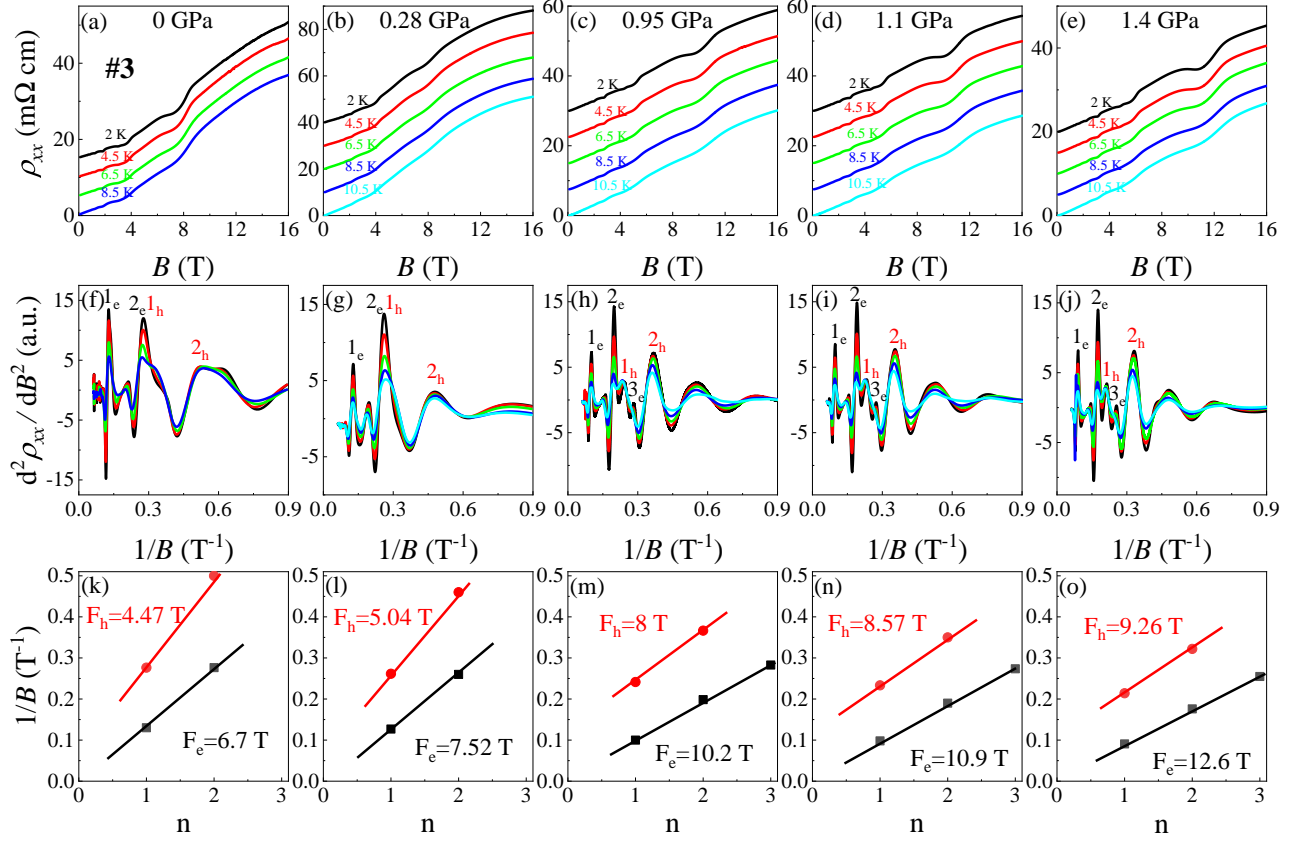


FIG. S4. **The Shubnikov de Haas(SdH) oscillations** (a)-(e) The magnetoresistance as a function of the magnetic field at different temperatures for $B \parallel c$ -axis under different pressure. (f)-(j) The oscillatory part of resistivity $d^2\rho_{xx}/dB^2$ for $H \parallel c$ -axis. (k)-(o) The Landau fan diagram derived from the field position of the distinct peaks of $d^2\rho_{xx}/dB^2$ for both the hole and electron pockets.

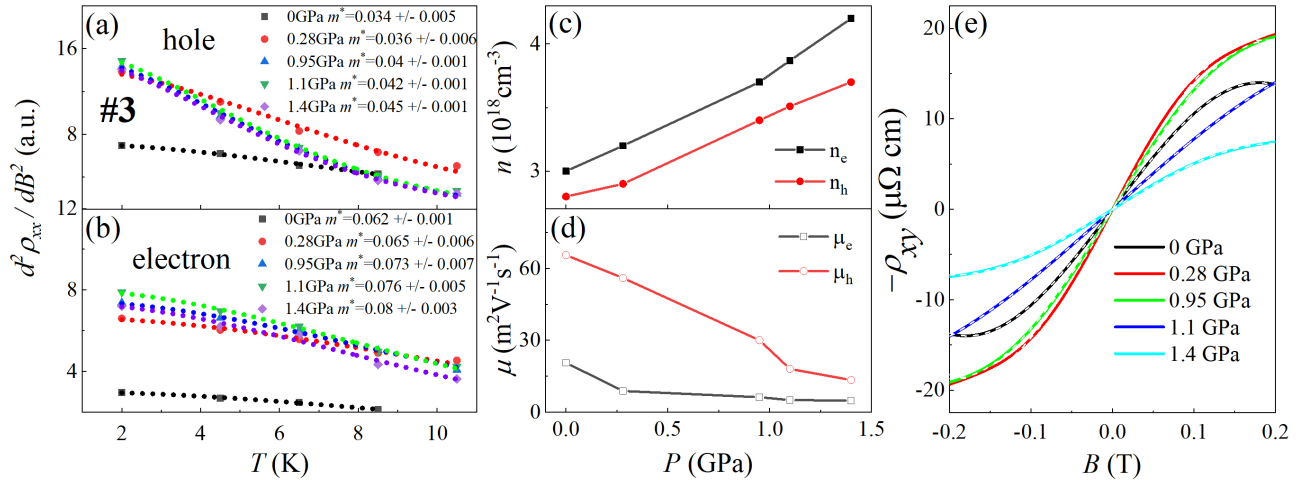


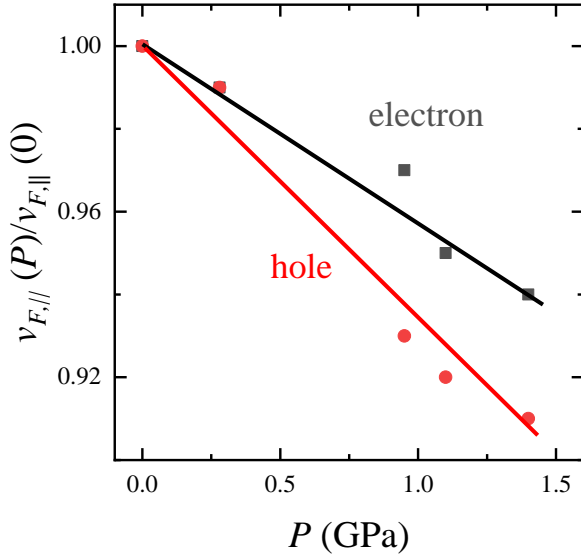
FIG. S5. **Pressure dependence of the effective masses, carrier density and mobility** : (a)(b) The L-K fitting with the effective masses of electron and hole at different pressure. (c)(d) The pressure dependence of carrier density and mobility with the pressure increases. (e) Hall resistivity under different pressure in low temperature. The dotted line represents a two-band fit to the data using the formula S1.

Pressure (GPa)	$k_{F,h,\perp}(nm^{-1})$	$k_{F,e,\perp}(nm^{-1})$	$m_{h,\perp}^*(m_0)$	$m_{e,\perp}^*(m_0)$	$k_{F,h,\parallel}(nm^{-1})$	$k_{F,e,\parallel}(nm^{-1})$	$m_{h,\parallel}^*(m_0)$	$m_{e,\parallel}^*(m_0)$
0	0.12	0.143	0.034	0.062	5.8	4.35	10	10
0.28	0.124	0.151	0.035	0.065	5.6	4.15	9.7	9.54
0.95	0.156	0.176	0.041	0.073	4.4	3.6	8.3	8.5
1.1	0.161	0.182	0.043	0.076	4.2	3.4	7.92	8.16
1.4	0.168	0.196	0.045	0.08	4	3.2	7.56	7.76

TABLE S2. The mass and the Fermi wave-vector of electrons and holes at different pressure.

γ_0	γ_1	γ_2	γ_3	γ_4	γ_5	Δ	ε_F	Ref.
3.2	0.397	-0.0202	0.29	0.132	0.0098	0.0221	-0.0223	[2]
2.85	0.3	-0.2	0	0	0	0.006	-0.026	[7]

TABLE S3. Band parameter sets for the SWM model.

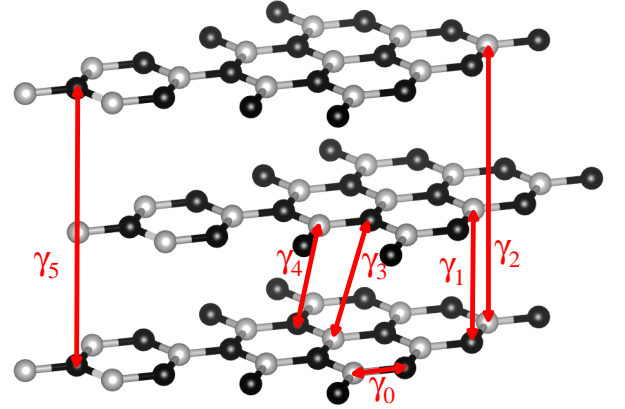
FIG. S6. Pressure dependence of the Fermi velocity $v_{F,\parallel} = \frac{\hbar k_{F,\parallel}}{m_{\parallel}^*}$ of electrons (black) and holes (red).

$$\begin{aligned}
& -0.5 \frac{\partial \ln |\gamma_2|}{\partial P} + 1.56 \frac{\partial \ln |\varepsilon_F|}{\partial P} + 0.057 \frac{\partial \ln |\Delta|}{\partial P} + 0.876 \frac{\partial \ln \gamma_1}{\partial P} \\
& + 0.01 \frac{\partial \ln |\gamma_5|}{\partial P} + 0.07 \frac{\partial \ln \gamma_4}{\partial P} = \frac{\partial \ln S_h}{\partial P} \quad (S8)
\end{aligned}$$

Following the same approximation as Brandt et al. [2]:

$$\frac{\partial \ln |\gamma_2|}{\partial P} = \frac{\partial \ln |\gamma_5|}{\partial P} = 2 \frac{\partial \ln \gamma_1}{\partial P}, \quad \frac{\partial \ln \gamma_3}{\partial P} = \frac{\partial \ln \gamma_4}{\partial P} \quad (S9)$$

we can determine the pressure dependence of m_e^* and m_h^* . The deduced pressure dependence and of the extremal cross section are shown in Table S4. They are all in good agreement with early works [2, 7, 9].

FIG. S7. **stacked graphite** The interaction between the carbon atoms are described by so-called the values of the parameters $\gamma_i (i = 0 - 5)$.

S5. THE PRESSURE DEPENDENCE OF DOS

Along the c -axis, the DOS for the lowest Landau levels follows: $E(k_z) = -2\gamma_2 \sin^2(\frac{c_0 k_z}{2})$ where γ_2 is the inter-layer hopping parameter between the two sub-lattices A and B and $c_0 = 6.7 \text{ \AA}$ [10]. It follows that: $\frac{dE}{dk_z} = -4\pi\gamma_2 \sin \pi\xi \cos \pi\xi$. Close to the transition the band along the c -axis is close to half-filling or so, $k_z \approx \frac{\pi}{2c_0}$ which gives at first order that: $\frac{dE}{dk_z} = -\pi\gamma_2$ which is a constant. This result reflects the fact that far from the extrema of the Landau level, the dispersion of the band along k_z is almost linear. The DOS is thus constant and only depends of γ_2 . Therefore B^* , like T^* , scales as γ_2 and thus with E_F . Note that this result is different in the case of a parabolic dispersion along k_z , where the DOS scales with $\sqrt{E_F}$ and not E_F . In this case we would have expect a distinct pressure dependence for T^* and B^* .

S6. THE BINDING ENERGY OF EXCITON

The exciton binding energy is given by $E_B = (\mu/m_0)(1/\epsilon^2)R_y$ [11, 12], where μ , m_0 , ϵ and R_y are the

	$d\ln S_e/dP$	$d\ln S_h/dP$	$d\ln m_e^*/dP$	$d\ln m_h^*/dP$
Itskevich <i>et al.</i> [8]	0.39			
Anderson <i>et al.</i> [7]	0.34 ± 0.06	0.4 ± 0.04		
Mendez <i>et al.</i> [9]				
Brandt <i>et al.</i> [2]	0.468 ± 0.01	0.485 ± 0.01	0.17 ± 0.03	0.24 ± 0.05
present work	0.467 ± 0.02	0.47 ± 0.03	0.182 ± 0.026	0.2 ± 0.06

TABLE S4. Comparison of the logarithmic derivatives of the SWM-model parameter, the extremal cross sections and of the effective mass with pressure (in GPa^{-1}) in early works [2, 7–9] and in this work.

exciton mass, the free electron mass, the dielectric constant and the Rydberg energy. Let's estimate its value in the case of graphite. By taking $m_{\parallel} = 5m_0$ [13], $m_{\perp} = 0.25m_0$ [14], $\epsilon_{\parallel} = 1.8225$ [15, 16] and the $\epsilon_{\perp} = 10$ [17], we found that, at zero pressure, $E_{B,\parallel} = 20.5\text{eV}$, $E_{B,\perp} =$

34meV . This exciton binding energy, is at least an order of magnitude larger than 10 K. Therefore, warming above 10 K destroys the order by crossing the Bose temperature of excitons (and not by unbinding the excitons).

-
- [1] Z. Zhu, H. Yang, B. Fauqué, Y. Kopelevich, and K. Behnia, Nernst effect and dimensionality in the quantum limit, *Nat. Phys.* **6**, 26 (2010).
- [2] N. B. Brandt, A. S. Kotosonov, S. V. Kuvshinnikov, and M. V. Semenov, Effect of pressure on the parameters of the energy spectrum of graphite, *Zh. Eksp. Teor. Fiz* **79**, 946 (1980).
- [3] A. N. Ramanayaka and R. G. Mani, Transport study of the berry phase, resistivity rule, and quantum hall effect in graphite, *Phys. Rev. B* **82**, 165327 (2010).
- [4] N. Brandt, S. Chudinov, and Y. G. Ponomarev, Modern problems in condensed matter sciences, Agranovich and AA Maradudin: North-Holland, Am-sterdam **20** (1988).
- [5] B. Fauqué and K. Behnia, Phase transitions induced by a magnetic field in graphite, in *Basic Physics of Functionalized Graphite*, edited by P. D. Esquinazi (Springer International Publishing, Cham, 2016) pp. 77–96.
- [6] N. B. Brandt, S. M. Chudinov, and Y. G. Ponomarev, eds., Chapter 8 - the effects of hydrostatic pressure on the electronic properties and energy spectrum of graphite and pyrocarbon materials, in *Modern Problems in Condensed Matter Sciences*, Vol. 20 (Elsevier, 1988) pp. 151–174.
- [7] J. R. Anderson, W. J. O'Sullivan, J. E. Schirber, and D. E. Soule, Effect of pressure on the Fermi surface of graphite, *Phys. Rev.* **164**, 1038 (1967).
- [8] E. S. Itskevich and L. M. Fisher, Vanishing of the shubnikov - de haas effect in a bismuth-antimony alloy under pressure, *Jetp Lett.* **5**, 114 (1967).
- [9] E. Mendez, A. Misu, and M. S. Dresselhaus, Magnetoreflexion study of graphite under pressure, *Phys. Rev. B* **21**, 827 (1980).
- [10] Y. Iye, P. M. Tedrow, G. Timp, M. Shayegan, M. S. Dresselhaus, G. Dresselhaus, A. Furukawa, and S. Tanuma, High-magnetic-field electronic phase transition in graphite observed by magnetoresistance anomaly, *Phys. Rev. B* **25**, 5478 (1982).
- [11] D. Jérôme, T. M. Rice, and W. Kohn, Excitonic insulator, *Phys. Rev.* **158**, 462 (1967).
- [12] B. I. Halperin and T. M. Rice, Possible anomalies at a semimetal-semiconductor transition, *Rev. Mod. Phys.* **40**, 755 (1968).
- [13] H. Yaguchi and J. Singleton, A high-magnetic-field-induced density-wave state in graphite, *J. Phys.: Condens.Matter* **21**, 344207 (2009).
- [14] J. Wang, P. Nie, X. Li, H. Zuo, B. Fauqué, Z. Zhu, and K. Behnia, Critical point for Bose–Einstein condensation of excitons in graphite, *Proc. Natl. Acad. Sci.* **117**, 30215 (2020).
- [15] E. Reyes, A. A. Krokhin, and J. Roberts, Effective dielectric constants of photonic crystal of aligned anisotropic cylinders and the optical response of a periodic array of carbon nanotubes, *Phys. Rev. B* **72**, 155118 (2005).
- [16] E. D. Palik, *Handbook of optical constants of solids*, Vol. 3 (Academic press, 1998).
- [17] Y. Iye, P. M. Berglund, and L. E. Mcneil, The magnetic field dependence of the critical temperature for the electronic phase transition in graphite in the quantum limit, *Solid State Commun.* **52**, 975 (1984).